Selective Oxidation of CH$_4$ to CH$_3$OH through Plasma Catalysis: Insights from Catalyst Characterization and Chemical kinetics modelling

Yanhui Yi,[1,2*#] Shangkun Li,[1, 2 #] Zhaolun Cui,[2] Yingzi Hao,[1] Yang Zhang,[3] Li Wang,[4] Pei Liu,[5] Xin Tu,[6] Xianming Xu,[7] Hongchen Guo,[1] and Annemie Bogaerts[2]

[1]State Key Laboratory of Fine Chemicals, School of Chemical Engineering, Dalian University of Technology, Dalian 116024, P.R. China.

[2]Research group PLASMANT, Department of Chemistry, University of Antwerp, Universiteitsplein 1, BE-2610 Wilrijk-Antwerp, Belgium.

[3]School of Materials Science and Engineering, Center of Advanced Analysis & Gene Sequencing, Zhengzhou University, Zhengzhou 450001, P. R. China.

[4]College of Environmental Sciences and Engineering, Dalian Maritime University, Dalian 116026, Liaoning, P. R. China.

[5]In-situ Center for Physical Sciences, School of Chemistry and Chemical Engineering, Shanghai Jiao Tong University, Shanghai 200240, P.R. China.

[6]Department of Electrical Engineering and Electronics, University of Liverpool, Liverpool, L693GJ, U.K.

[7]Daqing Chemical Research Center, China National Petroleum Corporation, Daqing 163714, P. R. China.

#: these authors contributed equally (shared first authors)

E-mail address: yiyanhui@dlut.edu.cn

ABSTRACT

The selective oxidation of methane to methanol (SOMTM) by molecular oxygen is a holy grail in catalytic chemistry and remains a challenge in chemical industry. We perform SOMTM in a CH_4/O_2 plasma, at low temperature and atmospheric pressure, promoted by Ni-based catalysts, reaching 81 % liquid oxygenates selectivity and 50 % CH_3OH selectivity, with an excellent catalytic stability. Chemical kinetics modelling shows that CH_3OH in the plasma is mainly produced through radical reactions, i.e., CH_4 + O(1D) → CH_3O + H, followed by CH_3O + H + M→ CH_3OH + M and CH_3O + HCO → CH_3OH + CO. The catalyst characterization shows that the improved production of CH_3OH is attributed to abundant chemisorbed oxygen species, originating from highly dispersed NiO phase with strong oxide support interaction with γ-Al_2O_3, which are capable of promoting CH_3OH formation through E-R reactions and activating H_2O molecules to facilitate CH_3OH desorption.

KEY WORDS: Methane Conversion; Plasma Catalysis; Selective Oxidation; Methanol Synthesis; Plasma Chemistry

1. Introduction

Methane (CH_4), abundant in natural gas, shale gas, coalbed gas, biogas and dry gas (i.e., emission of chemical industry), has become not only an important source of clean fossil energy, but also a feedstock for the chemical industry. At present, the industrial utilization of CH_4 is initiated by high temperature steam reforming to syngas (CO and H_2), which is then transformed into hydrocarbons through the Fischer-Tropsch process, or into methanol (CH_3OH), through a high-pressure reaction over Cu-Zn-Al catalyst. CH_3OH is a versatile molecule for the production of many bulk chemicals, such as ethylene, propylene and aromatics.[1] However, due to the strong C-H bond energy (439 kJ/mol), the negligible electron affinity and low polarizability of CH_4, as well as thermodynamic limitations, the syngas pathway is energy intensive and costly, which stimulates researchers to develop novel approaches for the conversion of CH_4. Thus, the selective oxidation of methane to methanol (SOMTM) is attracting more and more attention. [2, 3]

SOMTM is being studied by homogeneous catalysis, in strong acid media (sulfuric and trifluoroacetic acid), using complex catalysts with noble metals (Pt and Pd) as central atoms.[4-6] Alternatively, SOMTM can also be realized by impressive heterogeneous catalysis, e.g. iron-based zeolites [7, 8] and copper-based zeolites, [9-11] or supported noble metals, such as Au, Pd and Rh.[12, 13] However, numerous works in homogeneous or heterogeneous catalysis adopted high price oxidants such as N_2O or H_2O_2, which made this process economically infeasible in large-scale application. Using the abundant and cheap molecular oxygen (O_2) as oxidant, (R1),

67   would be highly desirable in industrial application.

68   $$CH_4 \ + \ 1/2 \ O_2 \ \rightarrow \ CH_3OH \qquad \triangle H^0_{298K} = -126.2 \ kJ \ mol^{-1} \qquad (R1)$$

69   SOMTM by O_2, R1, has been extensively studied. Colloidal Au-Pd nanoparticles

70   exhibited high CH_3OH selectivity (92%) in aqueous solution at mild temperatures on

71   SOMTM with H_2O_2 and O_2 as oxidants. More oxygenated products were formed than

72   the amount of H_2O_2 consumed, suggesting that the controlled breakdown of H_2O_2

73   activates methane, which subsequently incorporates molecular oxygen through a

74   radical process.[12] CeO_2/Cu_2O catalysts were able to activate methane at room

75   temperature, and water addition could generate centers on the catalyst surface with

76   special electronic properties, on which methane can directly interact to yield methanol.

77   [14, 15] Recently, highly active Au-Pd nanoparticles were encapsulated inside zeolites

78   and modified with a hydrophobic sheath, which can considerably enhance the oxidation

79   of methane to methanol.[16] The silanes appeared to allow diffusion of H_2, O_2, and CH_4

80   to the catalyst active sites, while confining the in-situ generated H_2O_2 decomposition,

81   which provided a high local peroxide concentration to facilitate methanol production,

82   with 17.3 % methane conversion and 92% methanol selectivity. Additionally, chemical

83   looping was also proposed to inhibit methane overoxidation on Cu- or Fe- containing

84   zeolite catalysts.[17]

85   Although great progress has been reported, SOMTM is, currently, still being

86   considered as a dream reaction in chemical industry and a holy grail in catalytic

87   chemistry. [3, 17, 18] Generally, it has to overcome two challenges, caused by

88   thermodynamics and kinetics, respectively. The first is how to improve the CH_3OH

89 selectivity. Thermodynamically, CH_3OH is not the favorable product, as CO and CO_2

90 are more stable than CH_3OH. Specifically, as shown in Figure S1, a low temperature (

91 $<$890 K) favors the production of CO_2 and H_2O, while a high temperature ($>$ 890 K)

92 favors CO and H_2. In other words, due to the higher reactivity of CH_3OH than the

93 feedstock CH_4, the catalytic sites, capable of oxidizing CH_4 into CH_3OH, can also

94 further oxidize CH_3OH into CO or CO_2 before CH_3OH can desorb from the catalyst

95 surface. The second challenge is how to reduce the kinetic energy barrier (Ea) of

96 SOMTM by O_2 at ambient conditions. The Ea of SOMTM by O_2 is much higher than

97 for SOMTM using N_2O or H_2O_2 as oxidants, because both N_2O and H_2O_2 can more

98 easily release an oxygen atom, as the main species to trigger the oxidation of CH_4 to

99 CH_3OH. Therefore, when using O_2 as oxidant, high temperature and high activity

100 catalysts are needed to overcome the Ea of SOMTM, which unfortunately leads to deep

101 oxidation.

102   One approach to overcome the above-mentioned challenges is a stepwise process,

103 i.e., stoichiometric chemical looping, which involves three separate steps: (1) activation

104 of the metal-zeolite catalyst by an oxidant at a relative high temperature (250-500 ^oC),

105 (2) methane reaction at a relative low temperature (25-200 ^oC), and (3) methanol

106 extraction using a solvent or steam at a relative low temperature (25-200 ^oC). [9, 19,

107 20] Currently, Cu and Fe exchanged zeolites have been extensively studied, and

108 significant attention was given to the elucidation of the nature of copper-oxo and iron-

109 oxo active sites. [17, 20] However, the state-of-the-art conversion of methane to

110 methanol via chemical looping stays a factor ~50 below the industrial threshold in an

111 overall production rate, and improvement on material productivity and decreased cycle

112 time are highly needed for this process.[21]

113   Another approach to overcome the above-mentioned challenges is plasma catalysis.

114 Non-thermal plasma (NTP), which is an ionized gas with clear non-equilibrium

115 character, offers a distinct approach to activate molecules by energetic electrons instead

116 of heat, and thus triggers chemical reactions at low temperature.[22-27] Generally, the

117 gas temperature in NTP remains near room temperature, while the generated electrons

118 exhibit a typical temperature of 1-10 eV ($\sim 10^4 - 10^5$ K), which is sufficient to activate

119 feed gas molecules (e.g., CH_4 and O_2) into reactive species, including radicals, excited

120 atoms and molecules, and ions. Several scientists have studied SOMTM by O_2 through

121 plasma and/or plasma catalysis, [28-36] but only a few have reported satisfying CH_3OH

122 selectivity. Nozaki applied a microplasma and obtained a CH_4 conversion to synthetic

123 fuels with maximum organic liquid selectivity of 70 % without catalysts (plasma alone),

124 [28] but the CH_3OH selectivity was below 15 %. Indarto realized CH_3OH synthesis

125 with optimum selectivity of 23 % using a dielectric barrier discharge (DBD) reactor

126 with Ni metal doped over yttria-stabilized zirconia as catalyst.[29] Chawdhury used a

127 packed bed DBD reactor, in which glass beads provided an optimal CH_3OH selectivity

128 of 35.4 %, [30] while further work reported the best CH_3OH selectivity of 37 % using

129 $CuO/\gamma-Al_2O_3$ catalyst.[31] Recently, $Cu/\gamma-Al_2O_3$, $Ni/\gamma-Al_2O_3$ and $Fe/\gamma-Al_2O_3$ catalysts

130 were compared for plasma-catalytic methane to value-added liquid fuels and chemicals,

131 in which the highest liquid oxygenate ($\sim 71\%$) were achieved, with $Fe/\gamma-Al_2O_3$ catalyst

132 exhibited highest methanol selectivity of 36.0% among three different catalysts.[32] In

133 addition, insights from microkinetic modelling for plasma-catalytic SOMTM process

134 were obtained on Pt(111) surface and the results showed that vibrational excitation and

135 especially radicals produced from CH_4/O_2 NTP could enhance the turnover frequency

136 (TOF) and improve the selectivity of CH3OH, HCOOH and C2 hydrocarbons. [33] In

137 general, this field is still in the early research stages and fundamental information on

138 the interaction of NTP with a catalyst is still lacking, and the limited CH_3OH selectivity

139 in most studies is attributed to the further oxidation of CH_3OH into CO and CO_2. [34]

140 Additionally, the reaction pathway for the production of CH_3OH and by-products

141 (HCHO, HCOOH, CO and CO_2) from CH_4 and O_2 in NTP is largely unknown.

142 Inspired by Lustemberg's work that Ni-CeO_2 catalysts shows excellent activity in

143 SOMTM at moderate conditions,[37] in this paper, we report SOMTM in a CH_4/O_2

144 plasma promoted by Ni-based catalysts, with 50 % selectivity to CH_3OH, and total

145 liquid oxygenates selectivity of 81 %, and with excellent catalytic stability. In addition,

146 we identify the underlying reaction mechanisms by combined experiments and

147 modeling.

2. Experimental section

2.1 Catalyst preparation

150 The catalysts were synthesized by the incipient wetness impregnation method

151 (Scheme S1). Commercial γ-Al_2O_3 pellets (1-2 mm diameter), synthesized by a

152 hydrothermal method, were calcined at 400 °C in a muffle oven for 5 hours before they

153 were used as supports. All analytical grade chemicals were purchased from Tianjin

154 Kemiou Chemical Reagent Co. Ltd. (Tianjin, China) and used without further

155   purification. The preparation procedure of the Ni catalysts is described in Scheme S2:

156   First, the precursor salt $Ni(NO_3)_2 \cdot 6H_2O$ was dissolved in deionized water, followed by

157   the addition of γ-Al_2O_3 pellets under stirring. After 12 hours aging at room temperature,

158   the sample was dried at 120 °C overnight. Finally, the sample was calcined by a muffle

159   oven at 540 °C for 5 hours in air condition, and the catalyst was noted as NiO/γ-Al_2O_3.

160   Varied nickel loading, i.e., 2, 6, 10, 15, 20, and 25 wt.% catalysts were synthesized

161   based above method.

162   **2.2 Experimental setup**

163   The experimental plasma catalysis setup is shown in Scheme S2. The plasma

164   catalytic SOMTM by O_2 was carried out using a coaxial DBD reactor with a novel

165   water electrode (grounding electrode) at atmospheric pressure. The DBD reactor

166   consists of a pair of coaxial quartz cylinders (inner and outer quartz tubes) in which a

167   stainless-steel (2 mm outer diameter) electrode was placed in the center, and circulating

168   water was pumped into the space between the inner and outer cylinder. A tungsten

169   filament is installed in between both cylinders to connect this circulating water (flowing

170   between this inner and outer wall) with a ground wire (outside of the reactor wall), so

171   that the circulating water acts as a ground electrode of our DBD. The flow rate (6 L/min)

172   and temperature of water was controlled by thermostatic baths with a circulation pump

173   and external temperature controller, which can effectively remove the heat generated

174   by the discharge and maintain a constant reaction temperature. The discharge length is

175   50 mm (defined by the length of the ground electrode, i.e., region of circulating water)

176   and the inner diameter of the inner quartz cylinder is 10 mm, yielding a discharge gap

177 of 4 mm. In the plasma catalysis experiments, the discharge space was fully packed by

178 1.25 g catalyst. CH_4 and O_2 were monitored by calibrated mass flow controllers and

179 mixed homogeneously before passing through the plasma reactor. Before igniting the

180 discharge, this gas mixture passed through the plasma reactor for about 10 minutes to

181 remove air, to ensure a safe operating procedure (outside the explosion limit). The

182 change of gas volume after the reaction was measured using a soap-film flow meter.

183 This is needed to quantitatively analyze the gas composition, and to achieve the exact

184 conversion (CH_4) and selectivity of the gaseous products (CO and CO_2). The discharge

185 voltage and current were detected by a digital phosphor oscilloscope (Tektronix, DPO

186 3012) with a high voltage probe (Tektronix P6015) and a current probe (Pearson 6585).

187   The feedstock and gas products were analyzed by an on-line gas chromatograph

188 (Tianmei GC-7900, TDX-01 column, Al_2O_3 packed column) with a thermal

189 conductivity detector (TCD) and a flammable ionized detector (FID). The liquid

190 products were cooled by a liquid trap (mixer of isopropyl alcohol and liquid nitrogen,

191 below -120 ºC) and then analyzed by GC-2014C (Shimadzu, PEG-2000 column), GC-

192 MS (Agilent 5975C, DB-1701 column), FTIR (ThermoFisher 6700) and ^{1}H-NMR

193 (Bruker AVANCE III 500). The reaction products, including H_2O, CO, CO_2, CH_3OH,

194 HCHO, HCOOH, $HCOOCH_3$, C_2H_5OH, CH_3CHO, and CH_3COOH, were analyzed

195 using external standards. The gas products were measured by gas chromatography,

196 while the liquid products were collected by a liquid trap and analyzed by GC, GC-MS,

197 FTIR and ^{1}H-NMR (Figure S2). The formulas of the standard calibrated concentration

198 curves are shown in Table S1. More details about qualitative and quantitative analysis

9

199   of products on CH_4/O_2 NTP could be found in supporting information. In this work, the

200   conversion of CH_4 and the selectivity of the gaseous products (CO_x, H_2 and C_2H_6) are

201   calculated as follows. Note that the selectivity of CO_x and C_2H_6 is calculated based on

202   carbon, while the selectivity of H_2 and H_2O is calculated based on hydrogen.

203   The CH_4 conversion was calculated by:

204   $X_{CH_4} (\%) = \dfrac{\text{moles of } CH_4 \text{ converted}}{\text{moles of initial } CH_4} \times 100\,\%$ (1)

205   The selectivity of the gaseous products was calculated as：

206   $S_{CO} (\%) = \dfrac{\text{moles of CO produced}}{\text{moles of } CH_4 \text{ converted}} \times 100\,\%$ (2)

207   $S_{CO_2} (\%) = \dfrac{\text{moles of } CO_2 \text{ produced}}{\text{moles of } CH_4 \text{ converted}} \times 100\,\%$ (3)

208   $S_{H_2} (\%) = \dfrac{\text{moles of } H_2 \text{ produced}}{2 \times \text{moles of } CH_4 \text{ converted}} \times 100\,\%$ (4)

209   $S_{H_2O} (\%) = 100\,\% - (S_{CH_3OH} + S_{HCHO} + S_{HCOOH} + S_{H_2} + S_{C_2})$

210   (5)

211   $S_{C_2H_6} (\%) = \dfrac{2 \times \text{moles of } C_2H_6 \text{ produced}}{\text{moles of } CH_4 \text{ converted}} \times 100\,\%$ (6)

212   The selectivity of the liquid products was calculated as follows:

213   Total selectivity of liquid products (%) = $100\,\% - (S_{CO} + S_{CO_2} + S_{C_2H_6})$ (7)

214   The selectivity of the various oxygenates, $C_xH_yO_z$, can be calculated as:

215   $S_{C_xH_yO_z} (\%) = \dfrac{X \times N_{C_xH_yO_z}}{\sum X_i N_i} \times \text{eq } 5$

216   (8)

217   Where $N_{C_xH_yO_z}$ represents the number of moles of various oxygenates in the

218   liquid fraction. Note that we define here the carbon-based selectivity, and thus, H_2O and

219   H_2O_2 are not included in this formula.

220   The corresponding yields of these $C_xH_yO_z$ oxygenates are calculated as:

221     $Y_{C_xH_yO_z} (\%) = S_{C_xH_yO_z} (\%) \times X_{CH_4} (\%)$ (9)

222 Finally, we defined the energy efficiency for CH_3OH formation (mol/kwh) as :

223   Energy efficiency $= \dfrac{\text{moles of methanol produced (mol/h)}}{\text{discharge power(kW)}}$ (10)

2.3 Catalyst characterization and NTP diagnostics

225   The structural properties of the $NiO/\gamma\text{-}Al_2O_3$ catalysts were investigated by X-ray

226 diffraction (XRD), conducted using a SmartLab 9kW diffractometer with Cu Kα

227 radiation (240 kV, 50 mA). The H_2-temperature programmed reduction (H_2-TPR) was

228 performed on a Quanta chrome ChemBET Pulsar Chemisorption instrument. Before

229 the analysis, the samples (0.20 g) were pretreated with He from ambient temperature to

230 150 $^{\circ}$C, and kept at 150 $^{\circ}$C for 60 minutes. Afterward, the samples were cooled to 50 $^{\circ}$C

231 in He atmosphere. Finally, the H_2-TPR was carried out in a flow of H_2/Ar mixture (120

232 ml/min, 10％ H_2) from 100 $^{\circ}$C to 1000 $^{\circ}$C at a heating rate of 10 $^{\circ}$C/min. X-ray

233 photoelectron spectroscopy (XPS) was conducted by Thermo Fisher ESCALAB XI^{+}

234 with Al Kα X-ray source. The C 1s binding energy value (284.8 eV) was taken as a

235 reference level. Nitrogen physisorption was conducted on a Micromeritics ASAP 2020

236 instrument at -196 $^{\circ}$C to obtain textural information. Prior to the measurement, the

237 samples were degassed at 400 $^{\circ}$C for 6 h. The surface area was calculated by the BET

238 method and the pore volume was obtained by the t-plot method. The chemical

239 composition of the $NiO/\gamma\text{-}Al_2O_3$ catalysts with various loading was analyzed by X-ray

240 fluorescence (XRF) on S8 TICER from Bruker AXS. Thermogravimetry was conducted

241 by Netzsch STA 449 F3 connected to a Balzers QMG 403D mass spectrometer. High-

242 resolution transmission electron microscopy (HRTEM) was conducted on Tecnai G2

243 F30 S-Twin with 300 kV accelerating voltage. High angle annular dark field scanning

244 transmission electron microscopy (HAADF-STEM) was performed by Titan^{3TM} G2 60-

245 300 with Cs-corrector configuration. The CH_4/O_2 NTP was investigated by optical

246 emission spectroscopy (OES) through a spectrograph (SP2758, Princeton instrument

247 company). A fiber was directly connected at the wall of the plasma reactor, to detect the

248 emission, which was analyzed by a spectrograph (750 mm, 300 G/mm gratings). A CCD

249 (PIXIS:400BR_eXcelon) was used to record the spectra with an on-line computer.

250 3 Results and discussion

251 3.1 Catalytic Performance

252   As shown in Figure 1A, the CH_4 conversion is zero when using only the $NiO/\gamma\text{-}Al_2O_3$

253 catalyst in the absence of NTP, indicating that SOMTM by O_2 cannot be triggered over

254 $NiO/\gamma\text{-}Al_2O_3$ catalyst without help of NTP. In plasma alone, 4.1 % CH_4 conversion is

255 achieved with 42.2 % CH_3OH selectivity, and no hydrocarbons have been detected by

256 the GC. Hence, plasma alone is able to quite selectively produce CH_3OH in our setup,

257 while it is generally stated in literature that it is not selective at all, and needs a catalyst

258 for the selective production of target compounds. [22, 34] This is attributed to the short

259 residence time, as will be explained by the modeling results below. Furthermore, the

260 influence of NTP (CH_4/O_2 molar ratio, temperature of grounding electrode, discharge

261 power and residence time) was also been studied, as shown in Figure S3-S6. After

262 packing by $\gamma\text{-}Al_2O_3$, the CH_4 conversion is slightly enhanced to 4.6 %, while the

263 CH_3OH selectivity is reduced to 41.4 %. However, when using $NiO/\gamma\text{-}Al_2O_3$ catalyst

264 (10 wt.% loading), the CH_4 conversion and CH_3OH selectivity increase to 6.4 % and

265 49.7 %, respectively, indicating that NiO/γ-Al$_2$O$_3$ catalyst has a positive effect on the

266 CH$_3$OH production in CH$_4$/O$_2$ NTP. The CH$_4$ conversion is still limited, attributed to

267 the short residence time of the gas inside the DBD reactor (high space velocity). By

268 tuning the flow rates and other discharge conditions, it should be possible to enhance

269 the conversion, but in this paper, we mainly focus on inhibiting the CH$_4$ overoxidation,

270 to increase the liquid oxygenates selectivity, especially for CH$_3$OH production. The

271 complete product distribution is shown in Figure S7 and S8, and the total selectivity of

272 liquid oxygenates reaches 80.7 %. This striking result is again attributed to the short

273 residence time, as illustrated by the modeling below.

274
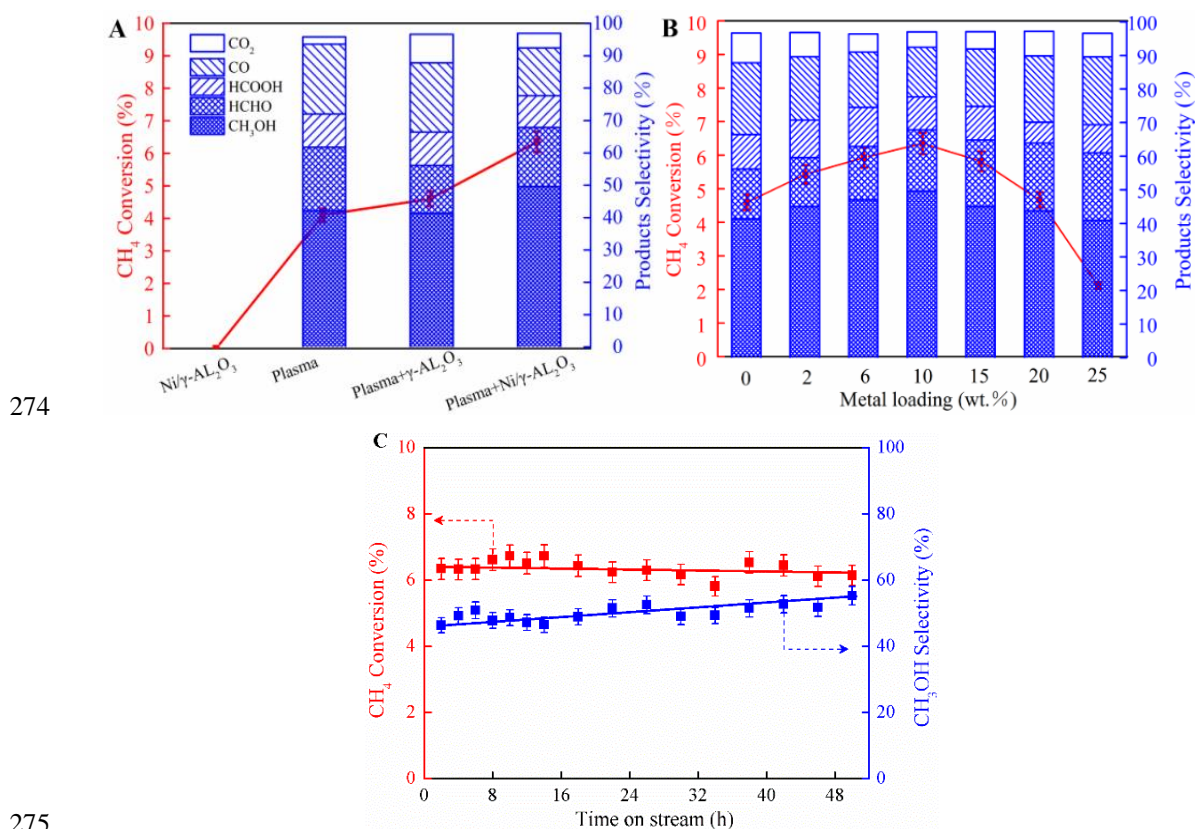
275

276 **Figure 1. Experimental results of SOMTM.** (A). CH$_4$ conversion and products

277 selectivity, using only NiO/γ-Al$_2$O$_3$ catalyst, only plasma, plasma with γ-Al$_2$O$_3$ beads,

278 and plasma with (10 wt.%) NiO/γ-Al$_2$O$_3$ catalyst (400 ml/min CH$_4$, 200 ml/min O$_2$,

279 85 °C circulating water, 1.25 g NiO/γ-Al$_2$O$_3$ catalyst, 30 W discharge power and 0.375

280 s residence time). (B). Effect of Ni loading on CH_4 conversion and products selectivity,

281 for plasma with $NiO/\gamma-Al_2O_3$ catalyst. (C). Stability test of the (10 wt.%) $NiO/\gamma-Al_2O_3$

282 catalyst in CH_4/O_2 NTP during 50 h continuous operation.

283   Furthermore, we studied $NiO/\gamma-Al_2O_3$ catalysts with varied loading (Figure 1B). The

284 highest CH_4 conversion and CH_3OH selectivity were both achieved at 10 wt.% loading.

285 Moreover, we operated the CH_4/O_2 NTP with 10 wt.% $NiO/\gamma-Al_2O_3$ catalyst

286 continuously for 50 hours, and the CH_4 conversion and CH_3OH selectivity remained

287 stable (Figure 1C), indicating the excellent catalytic stability of the $NiO/\gamma-Al_2O_3$

288 catalyst in CH_4/O_2 NTP for CH_3OH production. The results obtained in this paper have

289 been compared with those in literature. As shown in Figure 2A, the CH_3OH

290 productivity (27.3 mmol•g_{cat}^{-1}•h^{-1}) calculated by formula (1) of the SI is two orders of

291 magnitude higher than the best results obtained through stoichiometric chemical

292 looping using O_2 as the oxidant. [20, 38] As shown in Figure 2 B, the CH_3OH selectivity

293 is higher than the best results obtained through plasma catalysis, using various catalysts,

294 albeit at a lower CH_4 conversion. [30-32]
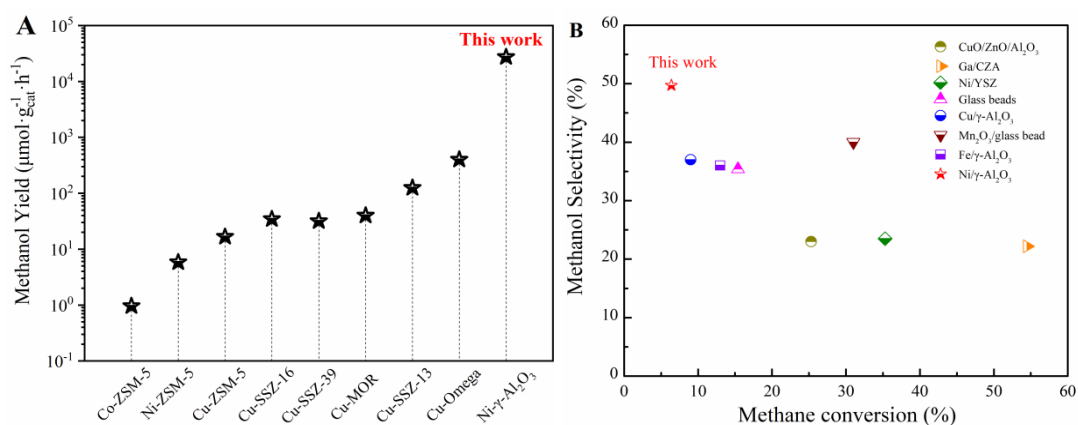
295

296 **Figure 2.** Comparison of this work with literature results. A: CH_3OH productivity by

297 stoichiometric chemical looping using O_2 as the oxidant, for different catalyst materials

298 (calculated based on the results adapted from references 20 and 38); B: CH_3OH

299　selectivity by plasma catalysis using O_2 as the oxidant (adapted from reference 30-32).

300

301　　　The hydrogen-based products selectivity is shown in Figure S9. The selectivity of

302　CH_3OH is almost 50 % in the case of "plasma + $NiO/\gamma\text{-}Al_2O_3$ catalyst, i.e., over 18 %

303　higher than in the case of plasma or plasma + $\gamma\text{-}Al_2O_3$ beads. The H_2 and H_2O

304　selectivities reach 5.6 % and 29.1 %, respectively, while the selectivities of HCHO and

305　HCOOH are around 9 % and 4.9 %, respectively, in the case of "plasma + $NiO/\gamma\text{-}Al_2O_3$

306　catalyst (10 wt.% loading).

307　　　Energy efficiency is a key performance indicator for plasma-catalytic SOMTM. We

308　defined the energy efficiency for CH_3OH formation by formula (7), in which the plasma

309　power was calculated through mathematical integration using the waveform of

310　discharge voltage (Figure S10) and discharge current (Figure S11). As illustrated by

311　Figure S12, the energy efficiency in the plasma-only case is 0.76 mol/kWh; it rises

312　slightly to 0.95 mol/kWh with $\gamma\text{-}Al_2O_3$, but with $NiO/\gamma\text{-}Al_2O_3$, it rises dramatically to

313　1.4 mol/kWh. Thus, while the CH_4 conversion and CH_3OH selectivity only increase by

314　2.3 % and 7.5 %, respectively, in case of plasma catalysis compared to plasma alone,

315　the energy efficiency rises by 84 %. Furthermore, the produced methanol with high

316　concentration (1.3 mol/L) in liquid can be condensed in the online cold-trap, without

317　further methanol extraction using a solvent or steam, which can avoid a stepwise

318　process on heterogeneous catalysis. This continuous operation condition under low

319　temperature and atmosphere pressure exhibited the great potential for plasma-catalytic

320　SOMTM by CH_4/O_2 NTP.

321　**3.2 Chemical kinetics modelling of CH_4/O_2 DBD plasma**

322   As mentioned above, in plasma alone, we achieved 42 % CH_3OH selectivity (Figure

323   1A), which is much better than most results in literature. [28-36] To explain this result,

324   we performed chemical kinetics modelling of CH_4/O_2 DBD plasma using

325   ZDPlaskin.[39] Details about the modelling, the species (Table S2) and reactions

326   (Tables S3-S5) in the model, are presented in SI.
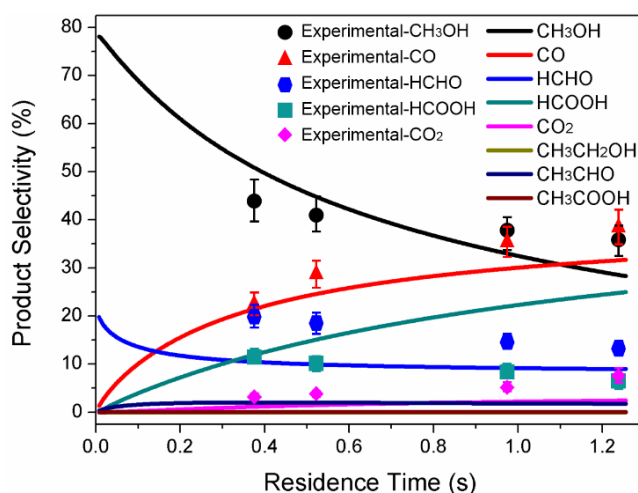
327

328   **Figure 3.** Products selectivity in CH_4/O_2 plasma, obtained by chemical kinetics

329   modeling (lines) and experiments (symbols) as function of residence time, for the same

330   conditions as in Figure 1.
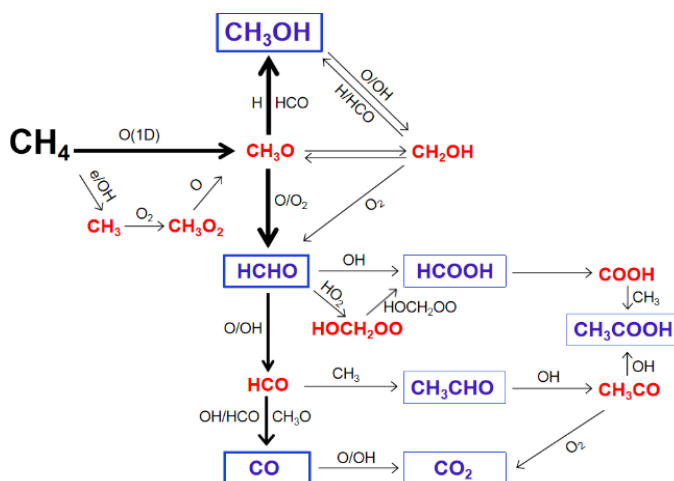
331

332   **Scheme 1.** Reaction pathways for the formation of CH_3OH and other oxygenates in the

333   CH_4/O_2 plasma, predicted by chemical kinetics modelling (ZDPlaskin). Red color

334   indicates reaction intermediates and blue color with rectangles means stable products.

335   The size of the products is approximately proportional to their selectivity and the

16

336 thickness of the arrow lines is proportional to the net rate of that reaction.

337   The lines in Figure 3 depict the calculated products selectivity as function of

338 residence time, derived from the densities of the species in the plasma (Figure S13).

339 Initially, the calculated CH_3OH selectivity is extremely high (~ 78 %), but it decreases

340 gradually upon increasing residence time, until about 30 % for a residence time of 1.2s.

341 HCHO exhibits a similar evolution (but with maximum selectivity around 20 %), while

342 CO, HCOOH and CO_2 exhibit the opposite trend. To verify the modelling, we

343 performed experiments at varying residence time (symbols in Figure 3). The

344 experimental selectivities of CH_3OH, HCHO, CO and CO_2 agree reasonably well with

345 the modelling results (similar trends), indicating that the model provides a realistic

346 picture of the formation of these products in the CH_4/O_2 plasma. For HCOOH, however,

347 the agreement is not yet satisfying, suggesting that important production or loss

348 processes for HCOOH might be missing in the model, or that their rate coefficients are

349 not correct, but we can only rely on the input data (chemical reactions and

350 corresponding rate coefficients) available in literature, and we don't want to tune the

351 model to fit it to the experiments without scientific basis. However, it means that our

352 model cannot yet be used to predict the reaction pathways for HCOOH, but we can use

353 it for the other possible reaction pathways in the CH_4/O_2 plasma. As shown in Scheme

354 1, CH_3OH is mainly produced from CH_3O species through the reactions $CH_3O + H +$

355 $M \rightarrow CH_3OH + M$ and $CH_3O + HCO \rightarrow CH_3OH + CO$.

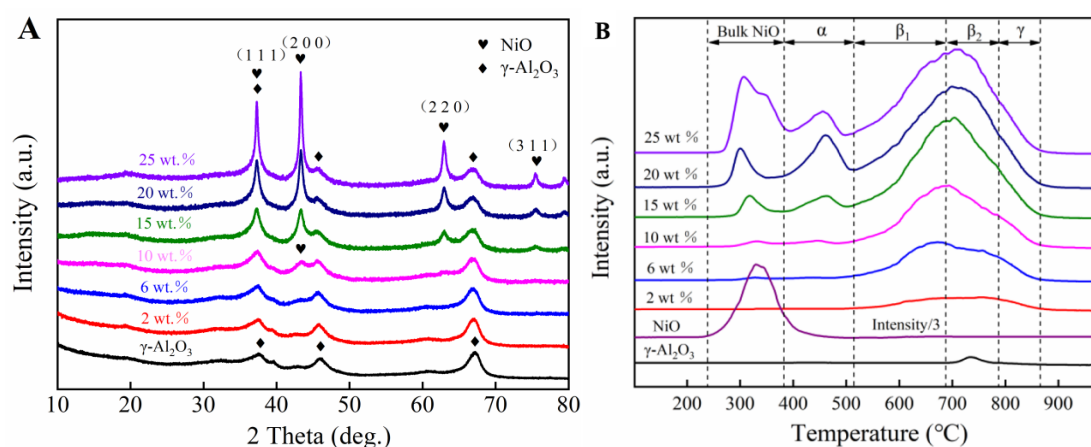356 **3.3 NiO/γ-Al$_2$O$_3$ Catalysts characterization**

357   In spite of the high CH_3OH selectivity at short residence time, the CH_4 conversion is

358 quite low (4.1 %), caused by the high space velocity. However, as shown in Figure 1,

359 the Ni catalyst (with 10 wt. % loading) enhances both the CH_4 conversion and CH_3OH

360 selectivity. It is very interested that both CH_4 conversion and CH_3OH selectivity

361 synchronously reached the highest value at 10 wt.% loading, since generally CH_3OH

362 selectivity decreases with the increase of CH_4 conversion. To reveal the unique role of

363 the Ni-based catalysts, we characterized them by XRD, HAADF-STEM, H_2-TPR, XPS,

364 HRTEM, XRF and N_2 physisorption.

365 The XRD result (Figure 4 A) reveals no evident NiO peak for Ni loadings below 10

366 wt.%, indicating the high dispersion of the NiO particles on γ-Al_2O_3. However, a group

367 of NiO diffraction peaks gradually appears upon increasing metal loading, showing the

368 formation of larger NiO particles. The NiO crystal size is estimated by the

369 Debye−Scherrer equation, presented in Table S6. It is observed that NiO particles on

370 NiO/γ-Al_2O_3 with Ni loading from 15 to 25 % are in the range of 10.3−22.1 nm. In

371 addition, the adsorption-desorption isotherm and pore size distribution curve of the

372 catalysts are shown in Figure S14, and the corresponding surface values are presented

373 in Table S6. Clearly, surface area of NiOγ-Al_2O_3 catalysts gradually declined with the

374 increasing of Ni loading, and γ-Al_2O_3 support shows the highest surface area (216.5

375 m^2/g). By correlating the surface area (Table S6) with the reaction performance (Figure

376 1), it can be concluded that surface area is not the key factor in determining catalytic

377 performance of NiO/γ-Al_2O_3 catalysts in DOMTM.

378 Figure 4 C, D and E show HAADF-STEM images of 2 wt.% NiO/γ-Al_2O_3, 10

379 wt.% NiO/γ-Al_2O_3 and 25 wt.% NiO/γ-Al_2O_3 catalysts, respectively. Clearly, the NiO

380 particle size in 2 wt.% NiO/γ-Al$_2$O$_3$ and 10 wt.% NiO/γ-Al$_2$O$_3$ is very small (< 5 nm),

381 but the size in 25 wt.% NiO/γ-Al$_2$O$_3$ is bigger (> 10 nm). Figure S15 shows the

382 HAADF-STEM mapping results of 6 wt.% NiO/γ-Al$_2$O$_3$, 15 wt.% NiO/γ-Al$_2$O$_3$ and 20

383 wt.% NiO/γ-Al$_2$O$_3$. It can be seen that NiO was uniformly dispersed in 6 wt.% NiO/γ-

384 Al$_2$O$_3$. In 15 wt.% NiO/γ-Al$_2$O$_3$ and 20 wt.% NiO/γ-Al$_2$O$_3$, however, NiO particles with

385 size more than 10 nm can be clearly observed. HRTEM images (Figure S16) show

386 similar results. These morphology results indicate that NiO was highly dispersed on the

387 surface of γ-Al$_2$O$_3$ with low loading (2, 6 and 10), and also demonstrate the larger NiO

388 particles at higher Ni loadings. Furthermore, a lattice space of 0.21 nm and 0.24 nm,

389 attributed to the (200) and (111) planes, was observed by HRTEM (Figure S17), and

390 similar results were also obtained from fast Fourier transformation (FFT) of NiO

391 particles in the HAADF-STEM images (Figure 4 C, D and E), consistent with the XRD

392 results (Figure 4 A).

393

19
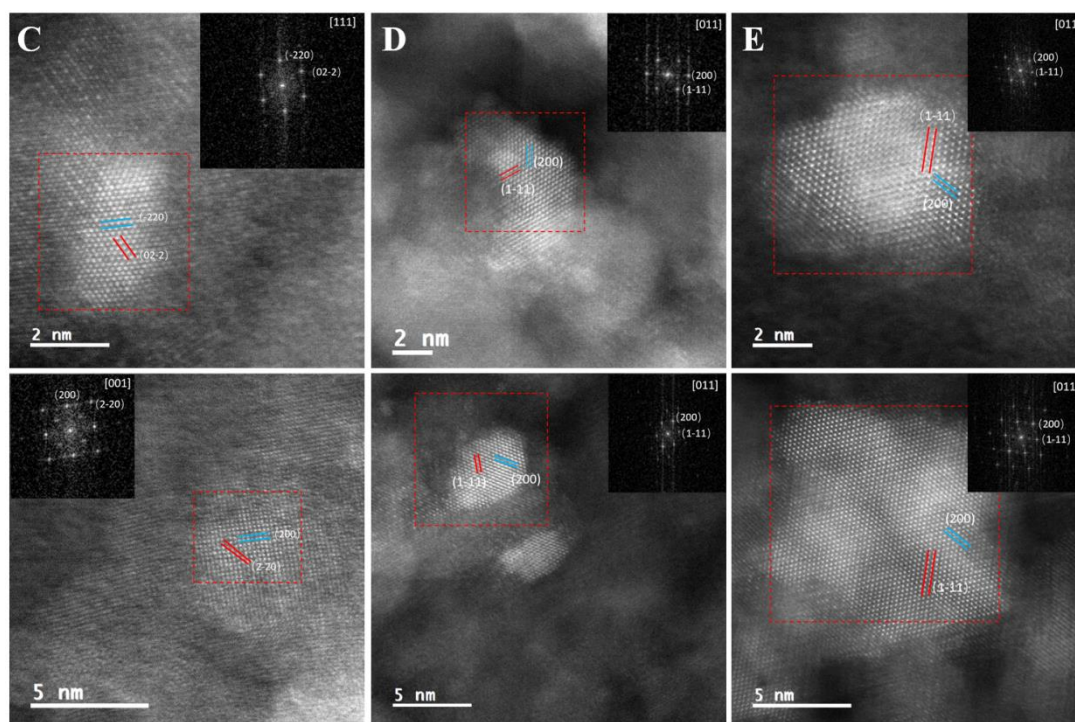
Figure 4. Characterization results of the NiO/γ-Al$_2$O$_3$ catalysts with varying loadings. (A) XRD patterns; (B) H$_2$-TPR profiles; (C) HAADF-STEM image of NiO/γ-Al$_2$O$_3$ catalyst with 2 wt.% loading; (D)HAADF-STEM image of NiO/γ-Al$_2$O$_3$ catalyst with 10 wt.% loading; (E) HAADF-STEM image of NiO/γ-Al$_2$O$_3$ catalyst with 25 wt.% loading.

The H$_2$-TPR profiles of the NiO/γ-Al$_2$O$_3$ catalysts are shown in Figure 4 B (NiO was used as a reference), and quantitative TPR results are presented in Figure S18 and Table S7. Five reducible peaks, at 280-350 °C, 390-510 °C, 510-690 °C, 690-790 °C and 790-840 °C, were detected, attributed to the reduction of five kinds of NiO species, i.e., bulk NiO (without interaction with Al$_2$O$_3$), α-type NiO (weak oxide-support interaction, WOSI), β$_1$-type NiO (strong oxide-support interaction (SOSI), with Ni abundant on surface), β$_2$-type NiO (SOSI, with Al abundant on surface) and γ-type NiO (nickel aluminum spinel; strongest interaction with Al$_2$O$_3$), respectively. [40-42] Obviously, β$_1$, β$_2$ and γ-type NiO are present in all NiO/γ-Al$_2$O$_3$ catalysts. On the other hand, α-type

410   and bulk NiO only appear for Ni loadings above 10 wt.%. This corresponds to the XRD

411   results, where obvious diffraction peaks of NiO (larger particles) were formed at high

412   loading (15%, 20% and 25%). This is also consistent with the morphology results,

413   where bigger NiO particles have been observed at high loading (15%, 20% and 25%).

414   The XPS profiles of the Ni 2p and O 1s of the NiO/γ-Al$_2$O$_3$ catalysts with various Ni

415   loadings are shown in Figure 5 A and B, respectively (Al 2p results are shown in Figure

416   S19). For Ni 2p, three peaks, corresponding to a binding energy at 854.0, 855.8 and

417   856.9 eV, have been detected. The low binding energy peak (854.0 eV) is assigned to

418   free-NiO species (big NiO particles). [43, 44] The moderate binding energy peak (855.8

419   eV) is usually attributed to NiO species with WOSI. [45] The high binding energy peak

420   (856.9 eV), however, generally results from NiO species with SOSI or Ni^{3+} species.

421   [44, 46] On the other hand, the intensity of the satellite peak of Ni^{3+} is extremely low

422   (it can nearly be ignored), which means that there is few Ni^{3+} species on the catalyst

423   surface, and thus the peak of binding energy at 856.9 eV is mainly attributed to NiO

424   species with SOSI.
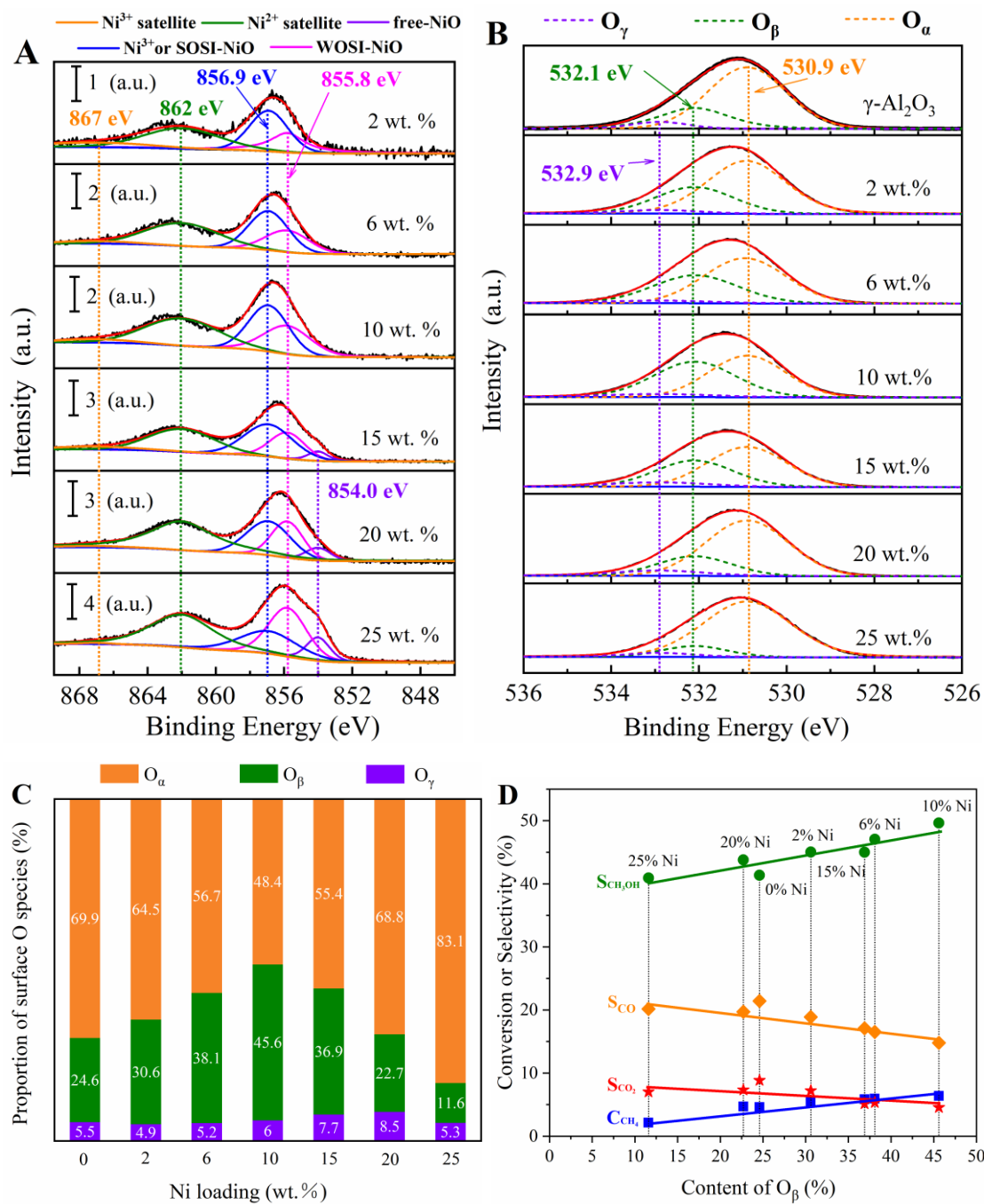
Figure 5. XPS results of the NiO/γ-Al₂O₃ catalysts with varying loadings. (A) Ni 2p region; (B) O 1s region; (C) Proportion of oxygen species for varied loading of Ni on γ-Al₂O₃; (D) Linear relationship between content of chemisorbed oxygen species ($O_β$) and reaction performance.

Furthermore, at low loading (2, 6 and 10 wt.%), Ni mainly exists as NiO species

433   with SOSI, since the peak of binding energy at 856.9 eV dominates the whole Ni 2p

434   peak. On the other hand, at higher loading (15, 20 and 25 wt.%), Ni mainly exists as

435   NiO species with WOSI and free-NiO, because the peak at 854.0 eV appears and the

436   contribution of the peak at 855.8 eV increases. The surface information obtained by

437   XPS analysis is consistent with the above XRD, TEM and H_2-TPR results.

438   The O 1s spectra of NiO/γ-Al$_2$O$_3$ catalysts presented in Figure 5 B can be fitted into

439   three peaks, corresponding to the lattice oxygen of metal oxide (O$_\alpha$), chemisorbed

440   oxygen (O$_\beta$), and adsorbed water or OH species (O$_\lambda$), with binding energy at 530.9 eV,

441   532.1 eV and 532.9 eV, respectively. [47, 48]

442   As shown in Figure 5 C, upon increasing Ni loading from 2 to 10 wt.%, the

443   proportion of O$_\beta$ species on the catalyst surface rises, and reaches the highest value

444   (45.6%) at 10 wt.% loading, and then it decreases. Interestingly, the variation trend of

445   Ni 2p peak of SOSI NiO (Figure 5 A) is synchronous with O 1s of O$_\beta$ species, which

446   means that the chemisorbed oxygen, i.e., O$_\beta$ species, mainly comes from the SOSI NiO.

447   Lattice oxygen, i.e., O$_\alpha$ species, are undoubtedly from crystals, i.e., γ-Al$_2$O$_3$ support,

448   free-NiO particles, and big NiO particles with WOSI. Upon increasing Ni loading, the

449   proportion of O$_\alpha$ species, however, firstly decreases and then increases, and the lowest

450   proportion was found at 10 wt.% loading, which means that the defects on the surface

451   of 10 wt.% NiO/γ-Al$_2$O$_3$ catalysts is much more than those of the other catalysts. The

452   defects have been created by SOSI, and usually, the created defects on metal oxide are

453   not stable. In an oxidizing atmosphere, they tend to combine with oxygen to form

454   chemisorbed oxygen, i.e., O$_\beta$ species. That is, NiO with SOSI leads to surface

455   chemisorbed oxygen species.

456   Figure 5 D presents the reaction performance (CH_4 conversion, CH_3OH selectivity,

457   CO and CO_2 selectivity) as a function of O_β content on the catalyst surface.

458   Interestingly, with increasing O_β species content, both CH_4 conversion and CH_3OH

459   selectivity rise linearly, while both CO and CO_2 selectivity decrease linearly. Therefore,

460   it can be reasonably inferred that chemisorbed oxygen, i.e., O_β species, are the real

461   active sites for CH_4 to CH_3OH conversion in this study. In contrast, lattice oxygen

462   species, i.e., O_α, may be the sites leading to deep oxidation to produce CO and CO_2

463   (Figure S20).

464   TG-MS results (Figure S21) shows very limited carbon deposition. In addition, the

465   fresh and spent $NiO/\gamma-Al_2O_3$ (10 wt.%) catalysts were compared by XRD (Figure S22),

466   H_2-TPR (Figure S23) and XPS (Figure S24), and no evident changes were observed.

467   These results demonstrate the excellent catalytic stability of $NiO/\gamma-Al_2O_3$ catalyst in

468   CH_4/O_2 NTP for CH_3OH production. Some other information of the $NiO/\gamma-Al_2O_3$

469   catalysts, i.e., the real loading, surface area and porosity, is shown in Table S6.

470   **3.4 NTP diagnostics and reaction mechanism**

471   OES diagnostics were employed to reveal some of the important plasma species

472   playing a role in CH_4/O_2 NTP for CH_3OH synthesis. As shown in Figure 6 and Figure

473   S25, CH (431.4 nm), H (656.3nm) and O (777.4 nm and 844.7 nm) were directly

474   identified, demonstrating the existence of CH, H and O species in the plasma. However,

475   also other reactive species are present in the plasma, which cannot be observed by OES.

476   Morgan and Erwin stated that CH_4 can be decomposed into CH_3, CH_2 and CH neutral

477 fragments. [49, 50] Based on a 1D fluid model, De Bie et al. predicted a probability of

478 producing CH_3, CH_2 and CH radicals in CH_4 DBD plasma of 79 %, 15 % and 5 %,

479 respectively.[51] A similar trend was predicted in a CH_4/O_2 DBD plasma, again by a

480 1D fluid model. [52] Therefore, we can assume that CH_3 is more abundant than CH_2

481 and CH in the CH_4/O_2 NTP. The reason why CH_3 was not detected by OES is because

482 its emission lines appear in the infrared region, which is out of the wavelength range of

483 our OES measurements. For the oxidative species, the lines at 777.4 nm and 844.7 nm

484 were detected by OES, attributed to deexcitation of O $(3p^5P)$ and O $(3p^3P)$ atoms,

485 respectively.[53] However, the pathways for activation of O_2 through inelastic

486 collisions with energetic electrons, as listed in Figure S26, indicate that the generation

487 of O (^1D) is easier than the generation of O $(3p^5P)$ and O $(3p^3P)$. [54, 55] The reason

488 why we did not detect O (^1D) by OES is that it is a metastable species with long lifetime,

489 which dissipates its internal energy by chemical reactions, instead of deexcitation.

490 Therefore, there will be abundant CH_3 radicals and O (^1D) atoms in the CH_4/O_2 NTP,

491 which confirms the reaction pathway in Scheme 1, triggered by O (^1D) and CH_3. The

492 above OES results show that, in CH_4/O_2 plasma, there are abundant CH_3, O (^1D) and H

493 radical species.
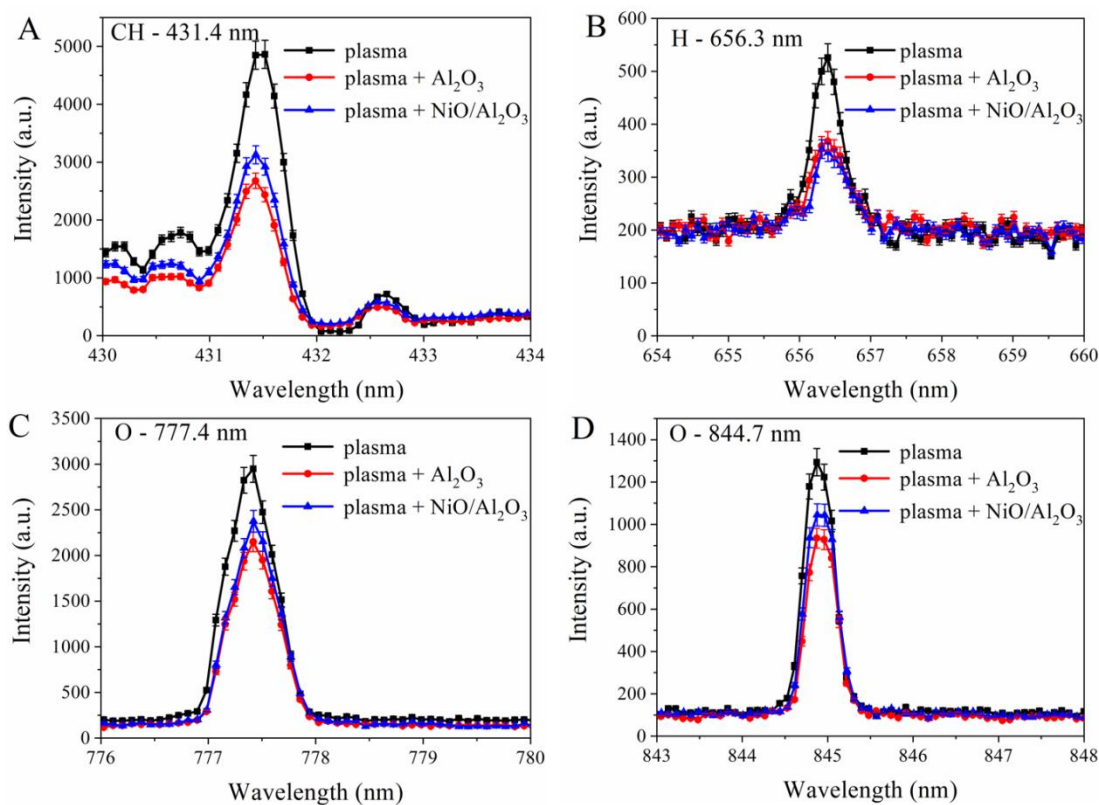
Figure 6. OES intensities of (A) CH (431.4 nm), (B) H (656.3 nm), (C) O (777.4 nm) and (D) O (844.7 nm), in the case of plasma alone, plasma + γ-Al_2O_3 beads, and plasma +(10 wt%) NiO/γ-Al_2O_3 catalyst, for the same conditions as in Figure 1.

Tang et al. predicted that CH_3OH synthesis usually proceeds through the Langmuir-Hinshelwood (L-H) mechanism in thermal catalysis.[56] In plasma catalysis, however, CH_3OH might be formed by both Eley-Rideal (E-R) and L-H mechanisms. [32, 57, 58] On the NiO/γ-Al_2O_3 (10 wt.%) catalyst surface, chemisorbed oxygen is abundant, which has been demonstrated by our XPS results. On the other hand, in the gas-phase, CH_3 and O radicals are also abundant, as proven by our OES results. Therefore, it can be reasonably assumed that CH_3O species can be formed, not only through radical reactions in gas-phase (proven by our modelling results in Scheme 1), i.e., $CH_3O_{(g)}$, but also through reaction between CH_3 in gas phase and chemisorbed

508   oxygen on the catalyst surface, i.e., $CH_3O_{(ad)}$. That is, due to the reactivity of the CH_3

509   radicals caused by their internal energy, the formation of CH_3O species through E-R

510   reaction between CH_3 radicals and chemisorbed oxygen will be very fast. Subsequently,

511   the formed CH_3O species may result in the generation of CH_3OH through

512   recombination with a H atom generated by CH_4/O_2 plasma (E-R reaction) [32].

513   Therefore, the reason why the $NiO/\gamma\text{-}Al_2O_3$ (10 wt.%) catalyst shows the best CH_4

514   conversion may be that it contains the highest content of chemisorbed oxygen. In the

515   case of plasma-catalytic CH_4 to CH_3OH conversion, the formation and desorption of

516   one CH_3OH molecule will consume one O_β species (as O_β is the real active site). In

517   conventional heterogeneous catalysis, this may lead to a continuous decrease of the O_β

518   content at the catalyst surface, and thus the reaction performance would decline since

519   the catalytic cycle cannot be completed. However, in the case of plasma catalysis, O_2 is

520   activated by the plasma into O atoms (either in ground or excited states, e.g., ^1D), which

521   are very reactive, and easily interact with the catalyst surface. So, we believe that these

522   O atoms are capable of interacting with the catalyst surface to rapidly form O_β species,

523   which compensates for the consumption of O_β species producing CH_3OH. In other

524   words, the plasma-generated reactive oxygen species enable the fast catalytic cycle for

525   CH_4 oxidation to CH_3OH.

526   The produced CH_3OH molecule usually strongly adsorbs on the catalyst surface,

527   making desorption difficult and resulting in deep oxidation, which is the key factor

528   inhibiting the CH_3OH selectivity, and it is the issue many researchers are concerning.

529   As reported by Lustemberg, water molecules can be activated by Ni/CeO_2 catalyst with

530   strong metal-support interactions, and then the activated H_2O molecule can promote

531   CH_3OH desorption.[37] In addition, Water molecular can act as a site blocker, which

532   can preferentially occupy the active Ce sites at the CeO_2-Cu_2O catalyst interface and

533   hinder methane overoxidation to CO and CO_2, meanwhile, it can also act as an active

534   center where the active *OH was produced at interfacial Ce sites to promote methanol

535   synthesis.[15] In the stepwise process using copper-exchanged zeolites, H_2O molecule

536   also plays an essential role in promoting CH_3OH formation and desorption.[59, 60]

537   Chemical kinetics modeling result (Figure S13) shows that H_2O molecules are abundant

538   in the CH_4/O_2 NTP. The measured products selectivity based on hydrogen (Figure S9)

539   shows that the selectivity of H_2O reached 29.1 %, demonstrating that H_2O molecules

540   are abundant in CH_4/O_2 NTP. As demonstrated by our XPS results (Figure 5), caused

541   by SOSI, the defects are also abundant at the interface between NiO particles and γ-

542   Al_2O_3 support, especially for the NiO/γ-Al_2O_3 catalyst with 10 wt.% loading. Therefore,

543   we believe that the H_2O molecule produced by CH_4/O_2 plasma can also be activated by

544   NiO/γ-Al_2O_3 catalyst with SOSI, and the activated H_2O molecule may promote

545   desorption of CH_3OH, which may be the reason why the NiO/γ-Al_2O_3 (10 wt.%)

546   catalyst shows the best CH_3OH selectivity. The role of plasma and Ni-based catalyst in

547   SOMTM has been summarized in Scheme 2.

548
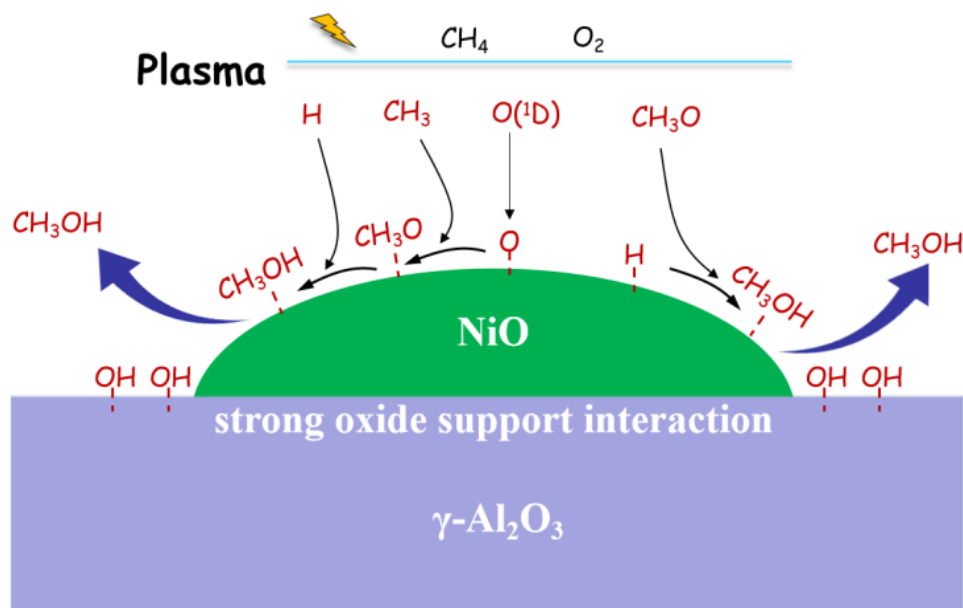
Scheme 2. Suggested reaction pathways of CH_3OH formation in CH_4/O_2 plasma promoted by NiO/γ-Al_2O_3 catalyst with SOSI (see text)

4. Conclusion

We demonstrated the selective oxidation of methane to methanol (SOMTM) in CH_4/O_2 plasma, promoted by Ni-based catalysts, with excellent catalytic stability. 76 % liquid oxygenates selectivity with 42 % CH_3OH selectivity are achieved in plasma alone, and the selectivities are further enhanced to 81 % and 50 %, respectively, when adding NiO/γ-Al_2O_3 catalyst with 10 wt.% loading. The energy efficiency by plasma catalysis is improved with 84 % comparing to plasma alone (from 0.76 to 1.4 mol/kWh).

In addition, chemical kinetics modelling shows that within the plasma, CH_3OH is mainly produced through radical reactions, i.e., $CH_4 + O(^1D) \rightarrow CH_3O + H$, followed by $CH_3O + H + M \rightarrow CH_3OH + M$ and $CH_3O + HCO \rightarrow CH_3OH + CO$. The catalyst characterization shows that the further improvement in CH_3OH production by plasma

catalysis is attributed to the highly dispersed NiO phase with SOSI. This causes an improvement of chemisorbed oxygen species, which catch CH_3 radicals from the plasma to form CH_3O_{ad} species. The latter can form CH_3OH through the ER reaction with H atoms from the plasma. Furthermore, H_2O molecules produced by CH_4/O_2 plasma may also be activated by $NiO/\gamma-Al_2O_3$ catalyst with SOSI, and the activated H_2O molecules may promote desorption of CH_3OH. The highest content of chemisorbed oxygen species can explain why the $NiO/\gamma-Al_2O_3$ catalyst with 10 wt.% loading shows both the best CH_4 conversion and the best CH_3OH selectivity.

Further work will be focused on enhancing the plasma-catalyst synergy through modifying the $NiO/\gamma-Al_2O_3$ catalyst by electronic promoters (multi-component catalysts), which should allow to enhance the adsorption capacity towards reaction intermediates (CH_3O, etc.) and the desorption of favorable target products, aiming to further improve the CH_4 conversion and CH_3OH selectivity.

ASSOCIATED CONTENT

Supporting Information. The supporting information is available free of charge via the Internet at XX.

Thermodynamic equilibrium of CH_4/O_2 conversion (Figure S1), preparation of catalysts (Scheme S1), experimental details for activity test (Scheme S2), results of qualitative analysis (Figure S2, Table S1), results of control experiments (Figure S3-S9), plasma diagnostics (Figure S10-S11), energy efficiency (Figure S12), details of chemical kinetic modeling (Table S2-S5, Figure S13), results of catalyst characterization (Table S6-S7, Figure S14-S24), OES diagnostic of CH_4/O_2 plasma

588   (Figure S25-S26).

AUTHOR INFORMATION

Corresponding Author

* E-mail: yiyanhui@dlut.edu.cn

Author Contributions

The manuscript was written through contributions of all authors. All authors have given approval to the final version of the manuscript.

Notes

The authors declare no competing financial interest.

ACKNOWLEDGEMENT

REFERENCE

[1] A. Caballero, P. Perez, Methane as raw material in synthetic chemistry the final frontier, Chem. Soc. Rev., 42 (2013), 8809-8820.

[2] J. Xie, R. Jin, A. Li, Y. Bi, Q. Ruan, Y. Deng, Y. Zhang, S. Yao, G. Sankar, D. Ma, J. Tang, Highly selective oxidation of methane to methanol at ambient conditions by titanium dioxide-supported iron species, Nature Catalysis, 1 (2018) 889-896.

[3] X. Meng, X. Cui, N.P. Rajan, L. Yu, D. Deng, X. Bao, Direct Methane Conversion under Mild Condition by Thermo-, Electro-, or Photocatalysis, Chem, 5 (2019) 1-30.

[4] R.A. Periana, D.J. Taube, E.R. Evitt, D.G. Loffler, P.R. Wentrcek, G. Voss, T. Masuda, A Mercury-Catalyzed, High-Yield System for the Oxidation of Methane to Methanol, Science, 259 (1993) 340-343.

[5] R.A. Periana, D.J. Taube, S. Gamble, H. Taube, T. Satoh, H. Fujii, Platinum Catalysts for the High-Yield Oxidation of Methane to a Methanol Derivative, Science, 280 (1998) 560-564.

[6] M. Muehlhofer, T. Strassner, W.A. Herrmann, New Catalyst Systems for the Catalytic Conversion of Methane into Methanol, Angew. Chem. Int. Ed. 41 (2002) 1745-1747.

[7] M.V. Parfenov, E.V. Starokon, L.V. Pirutko, G.I. Panov, Quasicatalytic and catalytic oxidation of methane to methanol by nitrous oxide over FeZSM-5 zeolite, J. Catal. 318 (2014) 14–21.

[8] C. Hammond, M.M. Forde, M.H. Ab Rahim, A. Thetford, Q. He, R.L. Jenkins, N. Dimitratos, J.A. Lopez-Sanchez, N.F. Dummer, D.M. Murphy, A.F. Carley, S.H. Taylor, D.J. Willock, E.E. Stangland, J. Kang, H. Hagen, C.J. Kiely, G.J. Hutchings, Direct catalytic conversion of methane to methanol in an aqueous medium by using copper-promoted Fe-ZSM-5, Angew. Chem. Int. Ed. 51 (2012) 5129-5133.

[9] M. H. Groothaert, P.J. Smeets, B.F. Sels, P.A. Jacobs, R.A. Schoonheydt, Selective Oxidation of Methane by the Bis(μ-oxo)dicopper Core Stabilized on ZSM-5 and Mordenite Zeolites, J. Am. Chem. Soc. 127 (2005) 1394-1395.

[10] S. Grundner, M.A. Markovits, G. Li, M. Tromp, E.A. Pidko, E.J. Hensen, A. Jentys, M. Sanchez-Sanchez, J.A. Lercher, Single-site trinuclear copper oxygen clusters in mordenite for selective conversion of methane to methanol, Nat. Comm. 6 (2015) 7546.

[11] D.K. Pappas, E. Borfecchia, M. Dyballa, I.A. Pankin, K.A. Lomachenko, A. Martini, M. Signorile, S. Teketel, B. Arstad, G. Berlier, C. Lamberti, S. Bordiga, U. Olsbye, K.P. Lillerud, S. Svelle, P. Beato, Methane to Methanol: Structure-Activity Relationships for Cu-CHA, J. Am. Chem. Soc. 139 (2017) 14961-14975.

[12] N. Agarwal, S. Freakley, R.U. McVicker, S.M. Althahban, N. Dimitratos, Q. He, D.J. Morgan, R.L. Jenkins, D.J. Willock, S.H. Taylor, C.J. Kiely, G.J. Hutchings1, Aqueous Au-Pd colloids catalyze selective CH_4 oxidation to CH_3OH with O_2 under mild conditions, Science 358 (2017) 223–227.

[13] J. Shan, M. Li, L.F. Allard, S. Lee, M. Flytzani-Stephanopoulos, Mild oxidation of methane to methanol or acetic acid on supported isolated rhodium catalysts, Nature, 551 (2017) 605-608.

[14] Z. Zuo, P.J. Ramirez, S.D. Senanayake, P. Liu, J.A. Rodriguez, Low-Temperature Conversion of Methane to Methanol on CeO_x/Cu_2O Catalysts: Water Controlled Activation of the C-H Bond, J. Am. Chem. Soc. 138 (2016) 13810-13813.

[15] Z Liu, E. Huang, I. Orozco, W. Liao, R.M. Palomino, N. Rui, T. Duchon, S. Nemsak, D.C. Grinter, M. Mahapatra, P. Liu, J.A. Rodriguez, S.D. Senanayake, Water-promoted interfacial pathways in methane oxidation to methanol on a CeO_2-Cu_2O catalyst, Science 368 (2020) 513–517.

[16] Z. Jin, L. Wang, E. Zuidema, K. Mondal, M. Zhang, J. Zhang, C. Wang, X. Meng, H. Yang, C. Mesters, F. Xiao, H_2O_2 Hydrophobic zeolite modification for in situ peroxide formation in methane oxidation to methanol, Science, 367 (2020) 193–197.

[17] M. Ravi, M. Ranocchiari, J.A. van Bokhoven, The direct catalytic oxidation of methane to methanol-a critical assessment, Angew. Chem. Int. Ed. 56 (2017) 16464-16483.

[18] X. Cui, H. Li, Y. Wang, Y. Hu, L. Hua, H. Li, X. Han, Q. Liu, F. Yang, L. He, X. Chen, Q. Li, J. Xiao, D. Deng, X. Bao, Room-temperature methane conversion by graphene-confined single iron atoms, Chem, 4 (2018) 1902-1910.

[19] P. Tomkins, M. Ranocchiari, J.A. van Bokhoven, Direct Conversion of Methane to Methanol under Mild Conditions over Cu-Zeolites and beyond, Accounts of chemical research, 50 (2017) 418-425.

[20] M.H. Mahyuddin, Y. Shiota, K. Yoshizawa, Methane selective oxidation to methanol by metal-exchanged zeolites: a review of active sites and their reactivity, Catal. Sci. Technol. 9 (2019) 1744-1768.

[21] J.P. Lange, V.L. Sushkevich, A.J. Knorpp, J.A. van Bokhoven, Methane-to-methanol via chemical looping economic potential and guidance for future research, Ind. Eng. Chem. Res. 58 (2019) 8674−8680.

[22] L. Wang, Y. Yi, H. Guo, X. Tu, Atmospheric pressure and room temperature synthesis of methanol through plasma-catalytic hydrogenation of CO_2, ACS Catal. 8 (2017) 90-100.

[23] J. Sentek, K. Krawczyk, M. Młotek, M. Kalczewska, T. Kroker, T. Kolb, A. Schenk, K.-H. Gericke, K. Schmidt-Szałowski, Plasma-catalytic methane conversion with carbon dioxide in dielectric barrier discharges, Appl. Catal. B: Environ. 94 (2010) 19-26.

[24] D. Li, V. Rohani, F. Fabry, A. Parakkulam Ramaswamy, M. Sennour, L. Fulcheri, Direct conversion of CO_2 and CH_4 into liquid chemicals by plasma-catalysis, Appl. Catal. B: Environ. 261 (2020) 118228.

683   [25] L. Wang, Y. Yi, C. Wu, H. Guo, X. Tu, One-Step Reforming of CO_2 and CH_4 into
684   high-value liquid chemicals and fuels at room temperature by plasma-driven
685   Catalysis, Angew. Chem. Int. Ed. 56 (2017) 13679-13683.

686   [26] C.E. Stere, J.A. Anderson, S. Chansai, J.J. Delgado, A. Goguet, W.G. Graham, C.
687   Hardacre, S.F. Rebecca Taylor, X. Tu, Z. Wang, H. Yang, Non-thermal plasma
688   activation of gold-based catalysts for low-temperature water-gas shift catalysis,
689   Angew. Chem. Int. Ed. 56 (2017) 5579-5583.

690   [27] R. Snoeckx, A. Bogaerts, Plasma technology - a novel solution for CO_2
691   conversion? Chem. Soc. Rev. 46 (2017) 5805-5863.

692   [28] T. Nozaki, A. Ağıral, S. Yuzawa, J.G.E. Han Gardeniers, K. Okazaki, A single step
693   methane conversion into synthetic fuels using microplasma reactor, Chem. Eng. J.
694   166 (2011) 288-293.

695   [29] A. Indarto, H. Lee, J.W. Choi, H.K. Song, Partial oxidation of methane with yttria-
696   stabilized zirconia catalyst in a dielectric barrier discharge, Energy Sources, Part
697   A: Recovery, Utilization, and Environmental Effects, 30 (2008) 1628-1636.

698   [30] P. Chawdhury, D. Ray, C. Subrahmanyam, Single step conversion of methane to
699   methanol assisted by nonthermal plasma, Fuel Process. Technol. 179 (2018) 32-
700   41.

701   [31] P. Chawdhury, D. Ray, T. Vinodkumar, C. Subrahmanyam, Catalytic DBD plasma
702   approach for methane partial oxidation to methanol under ambient conditions,
703   Catalysis Today, 337 (2019) 117-125.

704   [32] P. Chawdhury, Y. Wang, D. Ray, S. Mathieu, N. Wang, J. Harding, F. Bin, X. Tu,
705   C. Subrahmanyam, A promising plasma-catalytic approach towards single-step
706   methane conversion to oxygenates at room temperature, Appl. Catal. B: Environ.
707   284 (2021) 119735.

708   [33] B. Loenders, Y. Engelmann and A. Bogaerts, Plasma-catalytic partial oxidation of
709   methane on Pt(111): A microkinetic study of the role of different plasma species,
710   J. Phys. Chem. C, 125 (2021) 2966-2983.

711   [34] H. Puliyalil, D. Lašič Jurković, V.D.B.C. Dasireddy, B. Likozar, A review of
712   plasma-assisted catalytic conversion of gaseous carbon dioxide and methane into
713   value-added platform chemicals and fuels, RSC Adv. 8 (2018) 27481-27508.

714   [35] D.W. Larkin, L.L. Lobban, R.G. Mallinson, The direct partial oxidation of methane
715   to organic oxygenates using a dielectric barrier discharge reactor as a catalytic
716   reactor analog, Catal. Today 71 (2001) 199–210.

[36] L.M. Zhou, B. Xue, U. Kogelschatz, B. Eliasson, Partial oxidation of methane to methanol with oxygen or air in a nonequilibrium discharge plasma, Plasma Chem. and Plasma Process. 18 (1998) 375-393.

[37] P.G. Lustemberg, R.M. Palomino, R.A. Gutiérrez, D.C. Grinter, M. Vorokhta, Z. Liu, P.J. Ramírez, V. Matolín, M.V. Ganduglia-Pirovano, S.D. Senanayake, J.A. Rodriguez, Direct conversion of methane to methanol on Ni-Ceria surfaces: metal–support interactions and water-enabled catalytic conversion by site blocking, J. Am. Chem. Soc. 140 (2018) 7681-7687.

[38] A.J. Knorpp, A.B. Pinar, M.A. Newton, V.L. Sushkevich, J.A. van Bokhoven, Copper-exchanged omega (MAZ) zeolite: copper-concentration dependent active sites and its unprecedented methane to methanol conversion, ChemCatChem, 10 (2018) 5593-5596.

[39] S. Pancheshnyi, B. Eismann, G.J.M. Hagelaar, L.C. Pitchford, Computer code ZDPlasKin, http://www.zdplaskin.laplace.univ-tlse.fr, University of Toulouse, LAPLACE, CNRS-UPS-INP, Toulouse, France, 2008.

[40] X. Zhu, P. Huo, Y.-p. Zhang, D. Cheng, C. Liu, Structure and reactivity of plasma treated Ni/Al_2O_3 catalyst for CO_2 reforming of methane, Appl. Catal. B: Environ. 81 (2008) 132-140.

[41] D. Hu, J. Gao, Y. Ping, L. Jia, P. Gunawan, Z. Zhong, G. Xu, F. Gu, F. Su, Enhanced investigation of CO methanation over Ni/Al_2O_3 catalysts for synthetic natural gas production, Ind. Eng. Chem. Res. 51 (2012) 4875-4886.

[42] A. Alihosseinzadeh, B. Nematollahi, M. Rezaei, E.N. Lay, CO methanation over Ni catalysts supported on high surface area mesoporous nanocrystalline γ-Al_2O_3 for CO removal in H_2-rich stream, Int. J. Hydrog. Energy 40 (2015) 1809-1819.

[43] https://xpssimplified.com/elements/nickel.php.

[44] S. Kirumakki, B. Shpeizer, G. Sagar, K. Chary, A. Clearfield, Hydrogenation of naphthalene over NiO/SiO_2–Al_2O_3 catalysts: structure–activity correlation, J. Catal. 242 (2006) 319-331.

[45] C.P. Li, A. Proctor, D.M. Hercules, Curve fitting analysis of ESCA Ni 2p spectra of nickel-oxygen compounds and Ni/Al_2O_3 catalysts, Appl. Spectroscopy 38 (1984) 880-886.

[46] P. Salagre, J.L.G. Fierro, F. Medina, J.E. Sueiras, Characterization of nickel species on several y-alumina supported nickel samples, Journal of Molecular Catalysis A: Chemical 106 (1996) 125- 134.

[47] J. Jongsomjit, B. Jongsomjit, Catalytic ethanol dehydration to ethylene over nanocrystalline χ- and γ-Al$_2$O$_3$ catalysts., J. Oleo Sci. 66 (2017) 1029-1039.

[48] Y. Jian, T. Yu, Z. Jiang, Y. Yu, M. Douthwaite, J. Liu, R. Albilali, C. He, In-depth understanding of the morphology effect of α-Fe$_2$O$_3$ on catalytic ethane destruction. ACS Appl. Mater. Interfaces 11 (2019) 11369−11383.

[49] D.A. Erwin, J.A. Kunc, Electron-impact dissociation of the methane molecule into neutral fragments, Phys. Rev. A 72 (2005) 052719.

[50] D.A. Erwin, J.A. Kunc, Dissociation and ionization of the methane molecule by nonrelativistic electrons including the near threshold region, J. Appl. Phys. 103 (2008) 064906.

[51] C. De Bie, B. Verheyde, T. Martens, J. van Dijk, S. Paulussen, A. Bogaerts, Fluid modeling of the conversion of methane into higher hydrocarbons in an atmospheric pressure dielectric barrier discharge, Plasma Processes and Polym. 8 (2011) 1033-1058.

[52] C. De Bie, J. van Dijk, A. Bogaerts, The dominant pathways for the conversion of methane into oxygenates and syngas in an atmospheric pressure dielectric barrier discharge, J. Phys. Chem. C 119 (2015) 22331-22350.

[53] R.E. Walkup, K.L. Saenger, G.S. Selwyn, Studies of atomic oxygen in O$_2$ + CF$_4$ rf discharges by two-photon laser-induced fluorescence and optical emission spectroscopy, J. Chem. Phys. 84 (1986) 2668-2674.

[54] B. Eliasson, U. Kogelschatz, Electron impact dissociation in oxygen. J. Phys. B: At., Mol. Opt. Phys., 19 (1986) 1241-1247.

[55] P.C. Cosby, Electron-impact dissociation of oxygen, J. Chem. Phys. 98 (1993) 9560-9569.

[56] Q. Tang, Z. Shen, L. Huang, T. He, H. Adidharma, A.G. Russell, M. Fan, Synthesis of methanol from CO$_2$ hydrogenation promoted by dissociative adsorption of hydrogen on a Ga$_3$Ni$_5$(221) surface, Phys. Chem. Chem. Phys. 19 (2017) 18539-18555.

[57] M. Shirazi, E.C. Neyts, A. Bogaerts, DFT study of Ni-catalyzed plasma dry reforming of methane, Appl. Catal. B: Environ. 205 (2017) 605-614.

[58] S. Li, R. Ahmed, Y. Yi, A. Bogaerts. Methane to methanol through heterogeneous catalysis and plasma catalysis. Catalysts, 11 (2021) 590.

783 [59] V.L. Sushkevich, D. Palagin, M. Ranocchiari, J.A. van Bokhoven, Selective
784 anaerobic oxidation of methane enables direct synthesis of methanol, Science 356
785 (2017) 523–527.
786 [60] K. Narsimhan, K. Iyoki, K. Dinh, Y. Roman-Leshkov, Catalytic oxidation of
787 methane into methanol over copper-exchanged zeolites with oxygen at low
788 temperature, ACS central science, 2 (2016) 424-429.